

Synthetic Observations of Extremely High Velocity (EHV) SiO component in young molecular outflows

B. Vaidya^{1*}, Tom Douglas¹, Paola Caselli¹

¹*School of Physics and Astronomy, University of Leeds, Leeds LS2 9JT*

29 October 2013

ABSTRACT

A bipolar, collimated outflow is one of the first signposts of star formation. As it propagates through the molecular cloud, it injects energy and momentum via shocks and fosters chemical evolution by forming, destroying and entraining molecules along its path. High velocity molecular outflows are extensively studied for both low mass and high mass stars. They are usually observed using standard outflow and shocks tracers like CO and SiO. However, the exact nature of the excitation of these molecules is not yet clear due to lack of models that simultaneously study the dynamics along with complex molecular chemistry. For such a study, we have performed Magneto-hydrodynamic (MHD) simulations of knotty jet propagation into a molecular cloud using the PLUTO code. Firstly, we evolve the jet dynamical quantities in conjunction with different non-equilibrium cooling prescriptions of varying complexities. The most complex is that of molecular cooling along with H_2 chemistry. This prescription allows us to track the formation and destruction of HI, HII and H_2 along with the flow dynamics. The final state of the jet obtained for each cooling model is then given as an input to a radiative line transfer code to obtain SiO emission maps, spectra and position-velocity (PV) digrams. Our model can successfully explain the signatures of extremely high velocity (EHV) emission of SiO seen in early outflows. In particular, the line intensities, spectra and PV diagrams obtained from our model are very similar to ~~that~~ observed in case of outflows with EHV emission. In addition, the Atacama Large Millimeter Array (ALMA) predictions for such early molecular outflows shows bright emission coming from young internal knots and bow shock due to thermal instability. Our multi-line modeling of SiO supports the observational feature seen in Herbig-Haro (HH 211) that higher line transitions trace regions close to the axis of the jet. The dependence of emission on different cooling prescription and abundance profiles is clearly outlined from our parameter study.

Key words: MHD – methods:numerical – ISM: jets and outflows

1 INTRODUCTION

Jets are one of the first manifestations of star formation in dense molecular cores. They are ubiquitous in both massive and low mass star forming regions. These supersonic flows, perpendicular to the underlying accretion disk, play a vital role in removing excess angular momentum and thereby aiding in the accretion onto the protostar. For low mass stars, they are believed to be launched by magneto-centrifugally forces and further collimated by magnetic hoop stress (Blandford & Payne 1982; Konigl & Pudritz 2000). However, in case of high mass stars, radiative forces also contribute to flow dynamics during the later evolutionary

stages (Vaidya et al. 2011). Typically, these jets are few parsec in size long and can be divided into three length-scale domains, viz. source and disk scales ($1-10^2$ AU), envelope scales ($10^2 - 10^5$ AU) and parent cloud scales ($10^5 - 10^6$ AU) (REFERENCE: Frank et. al, 2013, PPVI). Of these, it is at the envelope scale where rich chemical evolution occurs as the jet interacts with the molecular medium. In this region, the jet propagates into a relatively static medium inducing shocks that are interesting from both a physical and chemical point of view. In addition to jets, molecular material from the surroundings is entrained and accelerated to high velocities giving rise to molecular outflows.

Bipolar molecular outflows from low and high mass stars have been studied in detail over the past decade (see reviews by Bachiller 1996; Beuther et al. 2002; Arce et al.

* E-mail: B.Vaidya@leeds.ac.uk (BV)

2007; Tafalla & Bachiller 2011). Advances in millimeter interferometer allow observations of these outflows with spatial resolution of few arc seconds. A large number of studies observing young outflows are done using standard outflow and shock tracers, e.g. CO and SiO respectively. In addition to these molecular tracers, shocks from these outflows are detected in molecular hydrogen using infra-red telescopes. Also, energetic outflows like that of Orion source I show evidence of SiO masers very close to the launching region of a MHD disk wind (Goddi et al. 2009; Vaidya & Goddi 2013). Based on these observational studies, various empirical properties for these outflows have been discovered. For example, the high resolution interferometric studies with CO (1-0) and SiO (2-1) have revealed highly collimated jet-like outflows (with opening angles less than a few degrees); they are referred to as *molecular jets*. HH 211 is the best example of such a molecular jet (Gueth & Guilloteau 1999). Episodic knots believed to be caused by variable accretion events are a common property of young molecular outflows usually observed with higher line transitions of CO and SiO (for e.g. in L1577: Gueth et al. 1998, in HH300: Arce & Goodman 2001a). These knots show their signatures as *wedges* in the PV diagrams Arce & Goodman (2001b). Also, observed in these outflows are signatures of rotation and *precision* (for e.g., in DG Tau: Bacciotti et al. 2002).

Even with a myriad of such empirical evidences, the exact nature of molecular emission in outflows is not clear. For a complete understanding it is imperative to complement these observations with theoretical models. Many models based on hydro-simulations and steady state shock calculations were proposed to explain the observational signatures of molecular outflows. Among them the two main models are that of wide-angled wind driven Shu et al. (1991) and jet driven outflow Canto & Raga (1991). The most popular among them is the jet driven model as wind driven molecular outflows not only fail to match observed PV diagrams (Cabrit & Bertout 1992) but also tend to sweep large quantity of material at the extremities of the lobes (Masson & Chernin 1992), while the jet driven models could successfully derive the global outflow shapes and mass velocity relations of CO outflows (Raga & Cabrit 1993; Masson & Chernin 1993; Downes & Cabrit 2003, 2007). There have also been some attempts to combine these two models into one (Shang et al. 2006) to explain the global observational features. However, most of these dynamical models do not account for shock chemistry. Instead, shock chemistry is studied independently using steady state non-dissociative C-type and dissociative J-type shocks models (Neufeld & Dalgarno 1989a; Schilke et al. 1997; Flower et al. 2003). The MHD calculations by Glassgold et al. (1991) suggested that molecules like SiO and CO could form within the jet. Similar conclusions of molecules surviving in steady state disk winds have also been shown (Panoglou et al. 2012). Very few simulations have modelled the outflow dynamics including molecular chemistry and in absence of magnetic fields (Raga et al. 1995; Smith & Rosen 2003). Recent models have also incorporated infall from the envelope (Rawlings et al. 2013) and radiation transfer (Offner et al. 2011) to explain molecular emission from Class 0 protostellar outflow sources.

In the present work, our goal is to take a step further in the modeling of jet driven molecular outflows. The present model aims to consistently derive observed emission proper-

ties of molecular outflows, specifically various SiO line transitions, by combining axisymmetric MHD simulations of radiative jet propagation with time-dependent simple chemistry and 3D radiative transfer. In particular, we evolve the jet dynamical quantities in conjunction with different non-equilibrium cooling prescriptions of varying complexities. The most complex is that of molecular cooling along with hydrogen chemistry. This prescription allows us to track the formation and destruction of HI, HII and H₂ along with the flow dynamics. The final state of the jet obtained for each cooling model is then given as input to a non-LTE line radiative transfer code to obtain emission maps, spectra and PV diagrams. These emission maps are further processed using the Common Astronomy Software Applications package (CASA) to obtain synthetic ALMA images of the resultant molecular outflows.

In the next three sections 2, 3 and 4, we describe our numerical setup, cooling prescriptions and radiative transfer code respectively. In sections 5 and 6, we will present results from the parameter survey and the discussions along with predicted ALMA maps will be presented in sections 7 and 8, followed by conclusions in section 9.

2 NUMERICAL SETUP

2.1 Numerical code and Equations

For our study, we carry out numerical axisymmetric ideal MHD simulations using the PLUTO code (Mignone et al. 2007) which is based on a conservative scheme of Godunov type. We have modified the original code to incorporate molecular cooling from self-consistent evolution of hydrogen chemistry (see Sect. 3).

In general, the MHD code considers the following set of equations. The conservation of the mass and the momentum,

$$\frac{\partial \rho}{\partial t} + (\vec{v} \cdot \nabla) \rho + \rho \nabla \cdot \vec{v} = 0 \quad (1)$$

$$\rho \left(\frac{\partial \vec{v}}{\partial t} + (\vec{v} \cdot \nabla) \vec{v} \right) = -\nabla P + \frac{1}{4\pi} (\nabla \times \vec{B}) \times \vec{B} \quad (2)$$

where ρ is gas density, \vec{v} the velocity vector, P the gas pressure, and \vec{B} the magnetic field vector with the poloidal and toroidal components - \vec{B}_p, \vec{B}_ϕ . Note that the forces due to gravity are neglected for this problem as the domain of interest is far away from the central object.

The cooling function Λ which depends on temperature T , mass density ρ and chemical abundances \mathbf{X} , appears in the energy equation as a source term,

$$\frac{\partial}{\partial t} (\rho E) + \nabla \cdot \left[\rho E \vec{v} + \left(P + \frac{B^2}{8\pi} \right) \vec{v} \right] - \vec{B} \cdot (\vec{v} \times \vec{B}) = -\Lambda(\rho, T, \mathbf{X}), \quad (3)$$

where the total energy density of the flow E comprises contributions from the internal energy ϵ , the mechanical energy and the magnetic energy,

$$E = \epsilon + \frac{v^2}{2} + \frac{B^2}{8\pi\rho}. \quad (4)$$

The gas pressure in the flow is related to the density ρ assuming an equation of state with the adiabatic index γ ,

$$P = (\gamma - 1)\rho\epsilon. \quad (5)$$

The evolution of chemical abundances for each species is solved via,

$$\frac{\partial \rho \mathbf{X}_i}{\partial t} + \nabla \cdot (\rho \mathbf{X}_i \vec{v}) = \rho \mathbf{S}_i, \quad (6)$$

where \mathbf{S}_i represents the net creation or destruction of a given species through chemical reactions (see Sect. 3).

The evolution of the magnetic field is governed by the induction equation,

$$\frac{\partial \vec{B}}{\partial t} = \nabla \times (\vec{v} \times \vec{B}). \quad (7)$$

In addition to the above set of equations, the code obeys the condition of divergence-free magnetic fields, $\nabla \cdot \vec{B} = 0$, which is numerically achieved by construction using the Powell's eight wave formulation (Powell et al. 1999).

2.2 Physical Model

We model the propagation of an axi-symmetric jet in (r, z, ϕ) cylindrical co-ordinates as it interacts with the ambient medium at distances $\gtrsim 1000$ AU. At these distances from the central source, the downward pull of gravity plays a negligible role on the dynamics of the jet. The ambient medium with which the jet interacts primarily represents the molecular cloud core. We study the interaction within a radial extent of $20 R_{\text{jet}}$ and a vertical extent of $100 R_{\text{jet}}$ (R_{jet} being the radius of the jet). Numerically, it is resolved by a uniform grid with a domain of 200×1000 cells in the radial and vertical directions. For simplicity, we choose this medium to be unmagnetized and non-turbulent. The density in the ambient medium varies with vertical height z as, $\rho_{\text{amb}} \sim (\rho_0/z^2)$ which is consistent with observations (Keto & Caselli 2010; Caselli 2011). The value of ρ_0 depends upon the density contrast, η , between the jet and the ambient medium. The number density in the jet is kept fixed such that the density in the ambient medium lies within a range of $10^4 - 10^5 \text{ cm}^{-3}$. The pressure in the ambient molecular medium is set so to maintain a constant temperature of 50 K. Note, dense molecular cores through which young outflows propagate have lower temperatures ranging from 10-20 K (Rathborne et al. 2007). As the jet is hypersonic in both cases, runs with lower ambient temperature of 10 K do not show any appreciable changes in final dynamical structure of the jet.

The jet enters into the medium through a nozzle of radius R_{jet} from the lower boundary ($z = 0$). Optically visible jets from T-Tauri stars are just about spatially resolved for the nearest star forming regions i.e, their radii are of order 100 AU at a few thousand AU from the source (Ray 2012). These jets have mass outflow rates of $10^{-7} M_{\odot} \text{ yr}^{-1}$ (Dougados et al. 2010). Younger and embedded jets in their Class 0 phase have outflow rates about 10-100 times higher than corresponding jets from optically visible young stars (Bally 2007; Dionatos et al. 2009; Ray 2012). Also, these optically obscure jets are relatively slower with velocities ranging around 100 km s^{-1} (Bally 2007) as compared to optically visible flows with velocities up to 500 km s^{-1} (e.g, Mundt et al. 1987). For the present model, the jet is injected into the domain with a velocity of $v_{\text{jet},0} = 100 \text{ km/s}$ and the jet density is set to 10^5 cm^{-3} within a jet radius of $2.5 \times 10^{15} \text{ cm}$. With these choices we obtain a mass outflow

rate of $10^{-6} M_{\odot} \text{ yr}^{-1}$. Most of the young outflows show variable features possibly due to variable accretion rates or internal shocks inside the jet (e.g. Bachiller 1996). We replicate such variability by superimposing the constant jet velocity with sinusoidal pulsation with an amplitude of 25 km s^{-1} with a periodicity of 70 yr such that the dense knots are separated by a distance of ~ 1000 AU.

Thermal and magnetic properties of jets from young stars are difficult to constraint because of their large variation not only within the jet but also in its surroundings. Forbidden line emissions from HH objects indicate excitation temperatures of the order of $\leq 10^4 \text{ K}$ (Podio et al. 2006; Bally 2007). However, in case of young jets the temperature is considerably lower (i.e, by an order of magnitude) than found in jets from Class I/II sources as derived from various atomic lines in molecular jets from L-1448C and HH 111 (Dionatos et al. 2009, 2010). The temperature at the jet nozzle for our model has been set to 1000 K. Thus, the jet is over-pressured by 60 times as compared with the ambient medium, assuming $\eta = 3.0$. Inside the jet beam, a radial variation of thermal and magnetic pressure is adopted to maintain a magneto-static equilibrium for all our runs (Stone & Hardee 2000). Based on these profiles, the toroidal magnetic field is assumed to be zero at the axis and achieves a maximum at radius, $r_m \sim 0.8 R_{\text{jet}}$ inside the jet. Though measuring magnetic fields in most jets is not possible via unpolarized nebular lines, in some special cases like HH 34S and HH 111V, it has been measured to be 10 and $30 \mu G$ respectively (Morse et al. 1993). Considering the dependence of such weak magnetic fields on density and radial distance in velocity-variable flows, Hartigan et al. (2007) has shown that at large distances from the star these fields only play a minor role in the dynamics. Thus for all our runs the value of magnetic field strength, $B_{\phi}(r_m)$ is set to be $\sim 37 \mu G$.

In order to consistently model the SiO emission arising from shocks as this jet interacts with the medium, we evolve the dynamics along with chemistry and cooling prescriptions. They are described in details in the next section.

3 CHEMISTRY AND COOLING

3.1 Molecular Chemistry

Typically, early collimated outflows have cooling times shorter than the dynamical times, implying that the radiative cooling plays a vital role in dynamics. In order to study such outflows it is necessary to evolve the dynamics in conjunction with full molecular chemistry and associated radiative processes. However, evolving a full complex network of chemical equations along with dynamics is a very computationally intensive task. As a result, we have focused only in evolving the chemical equations pertaining to atomic and molecular hydrogen. This prescription of molecular cooling has been added to the PLUTO code to study the chemical evolution of molecular outflows during the very early phases of star formation. In particular, the total hydrogen number density n_H comprises of contribution from atomic and molecular hydrogen i.e., $n_H = n_{H I} + n_{H_2}$. Whereas the contribution to electrons comes from the ionized hydrogen, $n_{H II}$ and from negligible but fixed fraction of metals ($Z \sim 10^{-4}$). Numerically, the non-homogenous parts of the equations 3

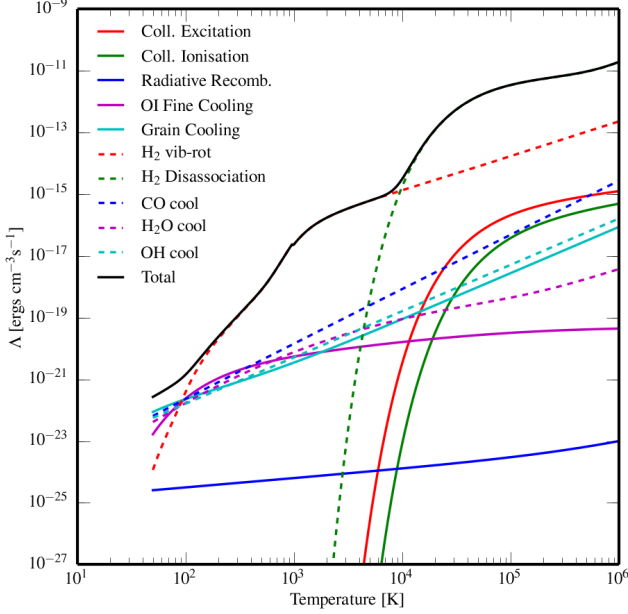


Figure 1. Variation of the cooling function $\Lambda(n, T, \mathbf{X})$ with temperature for the initial state.

and 6 are solved separately from the advection step using operator splitting. Further, the rate equations are evolved at each advection time step using sub-stepping and adaptive Runge-Kutta methods. The formation and destruction of fractions (denoted by \mathbf{X}_i in eq. 6) of three species, viz., fHI, fH₂ and fHII are tracked by the code based on the temperature dependent reaction rates whose coefficients are specified in the Table 1 along with their literature references.

3.2 Cooling Prescriptions

Figure 1 shows the variation of the cooling function, $\Lambda(\rho, T, \mathbf{X})$, with gas temperature assuming conditions of initial ambient density. Various processes that contribute to the cooling function in our model are listed in the figure. The formulations of these contributions are adopted from (Smith & Rosen 2003; O’Sullivan & Camenzind 2009, and references therein). For low temperatures, we also take into account contribution to cooling function from molecules like CO, whose abundance with respect to n_{H} is fixed to a value of 10^{-5} as measured in dense cores like L1544 (Keto & Caselli 2010). For each of the other molecules contributing to the cooling function (like OH, H₂O and atomic OI) the abundance is fixed to values of 5×10^{-6} . Note, the uncertain abundance values are rather arbitrary for these molecules. However, their contribution is only important when temperature is < 100 K as seen in figure 1. As the internal shocks, where most of the molecular hydrogen is produced maintain temperatures higher than 100 K and densities $\sim 10^6 \text{ cm}^{-3}$, cooling due to these molecules do not play a significant role even if the arbitrary abundance is increased by a factor of 10 (Smith & Rosen 2003). Instead, a substantial contribution to the cooling function, between $T = 100$ K and 3000 K, comes from the vibrational and rotational transitions of molecular hydrogen plays and a very crucial role during the jet evolution. Whereas, for temperatures above 3000 K the cooling is

mainly via H₂ disassociation. The total curve for the whole temperature range obtained in our runs is shown in black. The fact that the initial ambient medium is largely molecular, cooling is also dominated by molecular processes. In our reference model (see 5.2), we update this curve at each time step based on the fraction of various hydrogen species. Thus during the evolution, even contributions from collisional ionizations and excitations also become important in regions dominated by atomic and ionized hydrogen.

We also ran simulations of axisymmetric MHD jets with optically thin cooling prescriptions already existing in the public release of the PLUTO-4 code. They are power-law cooling, simplified non-equilibrium (or atomic) cooling and tabulated cooling. While these additional cooling prescriptions may not be a complete description of the chemical and radiative processes in early outflows, they are ideal to compare the results obtained from the more consistent newly added molecular cooling. In addition, we compare these radiative runs with an adiabatic jet to cover a wide spectrum of jet thermodynamics. Such a comparison is presented in section 6.1.

4 RADIATIVE TRANSFER

4.1 The radiative transfer code

The radiative transfer program used is LIME (Line Modeling Engine; Brinch & Hogerheijde 2010), which calculates line intensities based on a weighted sample of randomly chosen points in a continuous 3D model. The method of selecting these points is given in section 4.2. At each of these points, the density of the main collision partner (equivalent amount of H₂, given by $n(\text{H}_2) + n(\text{HI})$, assuming that ionized Hydrogen does not collide with SiO), gas temperature, velocity, molecular abundances and unresolved turbulent velocity are specified. These points are then smoothed by Lloyd’s algorithm (Lloyd 1982) in order to minimise the variation in distance between points whilst keeping the same underlying distribution. These points are then connected by Delaunay triangulation and it is between the points connected by this method that photon are allowed to propagate (fig. 2). The level populations of the selected molecules are calculated at each of these points from collisional and radiative (de)excitation and the local radiation field is calculated. This is repeated 20 times with the populations of each level converging towards a single value. This number of iterations is sufficient for the signal to noise ratio of the level populations (as defined in Brinch & Hogerheijde 2010) to exceed 1000 for 99% of the points, ensuring that the simulation has converged on a stable level population. After 20 iterations the model is ray-traced in order to produce synthetic brightness maps. The average of ten separate runs was taken to minimise the artefacts in the output images, resulting from the grid construction.

4.2 Grid construction

In order to construct the grid, candidate points are randomly selected from the volume to be simulated. These candidates then have their equivalent H₂ number density, and

Table 1. Summary of the chemistry reaction set. T is the temperature in Kelvin, T_{eV} is the temperature in electron-volts, $T_5 = T/1 \times 10^5$ and $T_2 = T/100$

No.	Reaction	Rate Coefficient (cm^3s^{-1})	Reference ^a
1.	$\text{H} + \text{e}^- \rightarrow \text{H}^+ + 2\text{e}^-$	$k_1 = 5.85 \times 10^{-11} T^{0.5} \exp(-157,809.1/T)/(1.0 + T_5^{0.5})$	1
2.	$\text{H}^+ + \text{e}^- \rightarrow \text{H} + \text{h}\nu$	$k_2 = 3.5 \times 10^{-12} (T/300.0)^{-0.8}$	2
3.	$\text{H}_2 + \text{e}^- \rightarrow 2\text{H} + \text{e}^-$	$k_3 = 4.4 \times 10^{-10} T^{0.35} \exp(-102,000.0/T)$	3
4.	$\text{H}_2 + \text{H} \rightarrow 3\text{H}$	$k_4 = 1.067 \times 10^{-10} T_{\text{eV}}^{2.012} (\exp(4.463/T_{\text{eV}}))^{-1} ((1. + 0.2472 T_{\text{eV}})^{3.512})^{-1}$	4
5.	$\text{H}_2 + \text{H}_2 \rightarrow \text{H}_2 + 2\text{H}$	$k_5 = 1.0 \times 10^{-8} \exp(-84,100/T)$	2
6.	$\text{H} + \text{H} \xrightarrow{\text{dust}} \text{H}_2$	$k_6 = 3.0 \times 10^{-17} \sqrt{T_2} (1.0 + 0.4\sqrt{T_2 + 0.15} + 0.2T_2 + 0.8T_2^2)$	5

^a REFERENCES – (1) [Cen \(1992\)](#) [Eq. 26a]; (2) [Woodall et al. \(2007\)](#) [UMIST Database] (3) [Galli & Palla \(1998\)](#) [Eq. H17]; (4) [Abel et al. \(1997\)](#) [Tab. 3 Eq. 13]; (5) [Hollenbach & McKee \(1979\)](#) [Eq. 3.8]

the number density of SiO, compared against those of a reference point in order to decide if the candidate point is to be used in the grid or not. Candidate grid points are selected at random in a cylindrical coordinate system that is linearly spaced in z and θ and logarithmically spaced in r . For each point to be selected, a random number α is drawn from the semi-open set $[0, 1)$ as a threshold. After selection of random coordinates, the H_2 density and SiO density at the candidate point (n and m , respectively) are compared against the densities of a reference point in the unperturbed ambient medium multiplied by a factor of $\frac{4\eta}{5}$ (n_{ref} and m_{ref}), where η is the density contrast between the jet and ambient medium. If $\alpha < \left(\frac{n}{n_0}\right)^{0.3}$ or $\alpha < \left(\frac{m}{m_0}\right)^{0.3}$ then the point is selected for use. Otherwise another r , θ , z co-ordinate is selected and it becomes the candidate point. In addition to this method of selection, 5% of the points are linearly distributed in x , y and z with no bias with regards to density or abundance. This provides a minimum level of sampling for the large low density regions in the outer parts of the simulated volume.

4.3 SiO abundance

Molecular abundance is one of the important ingredients that is required by the radiative transfer code described above. Typically, extremely low abundance of SiO is found ($n(\text{SiO})/n(\text{H}_2) < 3 \times 10^{-12}$) in dark, dense clouds such as TMC1 ([Ziurys et al. 1989](#); [Martin-Pintado et al. 1992](#)). Whereas, in outflows like L1448, SiO abundance can increase up to 10^{-6} especially in molecular bullets moving with a projected velocity of 60 km s^{-1} ([Dutrey et al. 1997](#)). Thus, there is an increase of 6 orders of magnitude from quiescent clouds to outflows. Production of gaseous SiO due to slow C-type shocks has been suggested to occur via release of silicon from grain cores and from grain mantles. Various stationary shock models indicate a sudden abundance increase in SiO near a shock speed of $20\text{--}30 \text{ km s}^{-1}$. However, several young outflows have velocities of the order of 100 km s^{-1} as in the present case. Shocks due to such outflows will dissociate H_2 and will become J (*jump*) type shocks. Thus, molecules observed in such energetic outflows must have been reformed in the flow as suggested by detailed models of J-shocks by [Neufeld & Dalgarno \(1989b\)](#). SiO formation in J shocks has also been modelled recently and has thought to be the source

of the SiO line emission observed in molecular outflows and jets ([Guillet et al. 2009](#)).

In spite of all numerical models relating to the study of enhancement of SiO in shocks, very little is known about the dependence of SiO abundance on shock speeds. Considering the complex grain chemistry that is involved in order to estimate the functional dependence of SiO abundance on shock speeds, we prescribe these profiles based on limited empirical evidences. The most simple among them is the top hat profile in which the SiO abundance is a low value of 10^{-12} below 20 km s^{-1} and above 100 km s^{-1} and a maximum value of 10^{-6} between these two velocities. Shock velocities $> 100 \text{ km s}^{-1}$ can lead to the ionisation of hydrogen and thereby effectively reduce the number of collision centers for SiO resulting in a weaker emission. However, we also consider a step function dependence of SiO abundance on shock velocity to incorporate cases where we allow for reformation of atomic and molecular species. In order to get rid of a discontinuous change of abundance, we also prescribe a gaussian such that the peak SiO abundance of 10^{-6} is at 60 km s^{-1} , while the value of $n(\text{SiO})/n(\text{H}_2)$ falls below 10^{-9} at 20 and 100 km s^{-1} . Such a huge variation in SiO abundance may indeed be the case in regions where SiO is seen in widespread (e.g., [Lefloch et al. 1998](#), also see section 8). Also along with a Gaussian profile, we consider the case where we extent the abundance of 10^{-6} beyond 60 km s^{-1} . These functional dependences of SiO abundance on shock velocity are shown in figure 3. In addition to this, if the temperature at the point is greater than $92,000 \text{ K}$ (the temperature of the Si-O bond disassociation energy) the abundance is reduced to 0.

Further, the velocities obtained from the dynamical simulations are in fact the jet flow velocities. They can well be different from the shock velocities depending upon the density contrast between the jet and ambient medium. For the present study, we will consider two cases. Firstly, the most simple one in which the jet flow velocity is same as the shock velocity. Considering that there is a density contrast in the simulation setup, this assumption will overestimate the shock velocity. We also consider a case in which the shock speed of a dense plug accumulated between the jet and medium is estimated by balancing the respective ram pressures ([Masson & Chernin 1993](#)),

$$v_s = \frac{v_{\text{jet}}}{1 + \eta^{-0.5}} = v_{\text{jet}} \delta \quad (8)$$

where v_s is the velocity of dense plug and v_{jet} is the jet

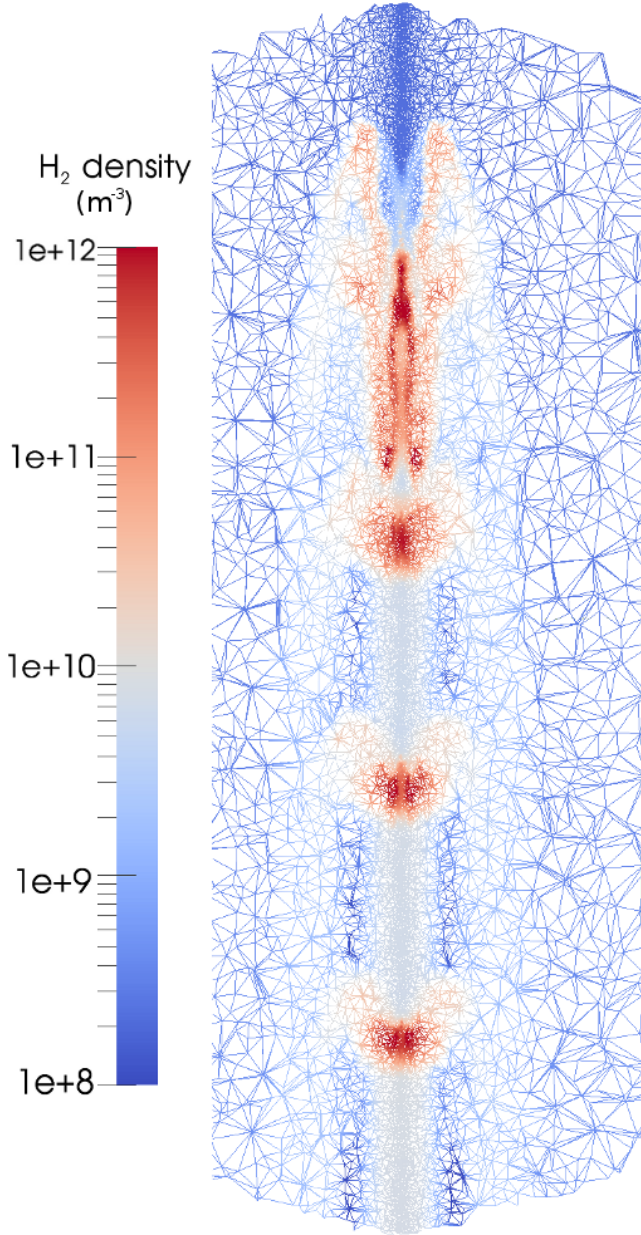


Figure 2. A plot of the points selected by the gridding process and the paths down which photons can propagate for points in the r, z plane. The points are color coded by the density distribution (in m^{-3} , as used in LIME) and are more concentrated in the high density knots.

velocity. A comparative view of using such velocity corrections and functional forms of SiO abundances are discussed in Sec 6.4.

5 PARAMETER SURVEY

The results and analysis for the present work are divided in two parts, viz., the dynamical numerical simulations and the radiative transfer analysis. For each part we have used certain parameters and the effect of changing them is studied. Ideally all these parameters should come from observational results. However, not all quantities needed for our study are

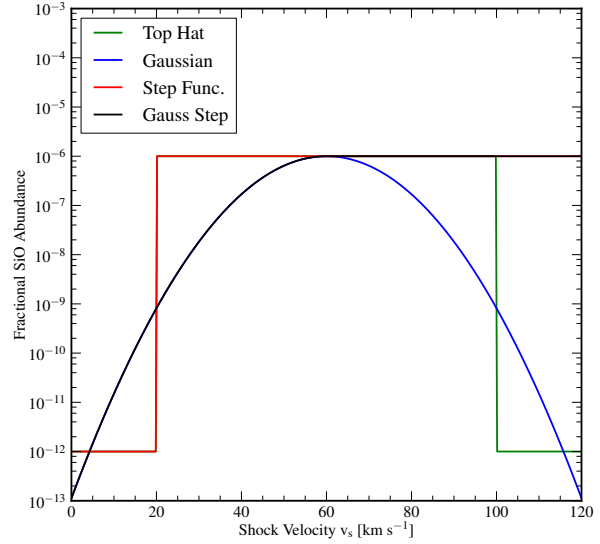


Figure 3. The different fractional SiO abundances as a function of shock velocity, v_s .

well constrained by observations, thus they are considered as free parameters. Such a parameter survey provides better handle on the range of allowed values on qualitative comparison with observations.

5.1 Parameter definitions

For the first part of the study concerning the dynamical numerical simulations, we will focus on two main parameters. They are the prescription of cooling and the density contrast between the jet and the ambient medium denoted by η . The various cooling prescriptions used for the present study are described in detail in section 3. They differ in the physical process that is responsible for cooling and chemistry. The most simple one is that of power-law cooling with no chemistry and the most complex cooling module is where molecular hydrogen chemistry is evolved with contributions to cooling from other abundant molecules like CO, OH etc.

A value of $\eta > 1$, means that that jet is over dense with respect to the medium. In all our runs with different cooling prescriptions, we have assumed the jet to be over-dense by 10 times compared to the ambient medium. Additionally, for the atomic, tabulated and molecular cooling runs (see section 3 for description of different cooling prescriptions) we have also used a value of η of the order of unity indicating similar densities in the jet and the medium. Table 2 lists all the runs with varying η and cooling prescriptions, along with the peak intensity and line widths at the bow shock.

To obtain the SiO emission maps and corresponding spectra, two additional free parameters are required along with other inputs described in section 4. They are the fractional abundance profile of SiO and the angle of inclination with respect to line of sight denoted by ϕ . Section 4.3 describes all the profiles used for the present study. $\phi = 90^\circ$ indicates that the outflow is in the plane of the sky. Additionally, we have used two other angles of inclination apart

from the plane of the sky, i.e., $\phi = 45^\circ, 60^\circ$ to compare results with observations. The runs with different fractional abundance profiles are described in table 3. A parameter introduced here is δ which is essentially the ratio of shock velocity v_s and physical jet velocity v_{jet} such that its value depends on density contrast η (see Eq. 8).

5.2 Reference Run

We define a reference run in order to quantify and compare results obtained from such a survey of above mentioned parameters. The results shown in this work will be pertaining to the reference run (unless otherwise mentioned) and appropriate comparison will be discussed with other runs.

The reference run in our calculation has density contrast $\eta = 3$ with the initial jet density of 10^5 cm^{-3} . This jet enters the ambient medium with a velocity of $v_{\text{jet},0} = 100 \text{ km s}^{-1}$ which is further superimposed by sinusoidal perturbations to replicate dense knots. The maximum value of toroidal magnetic field is set to be $37 \mu G$ at the base of the jet. Dionatos et al. (2009) have detected atomic lines towards a molecular jet from L1448-C indicating a presence of embedded atomic jet at low excitation. Additionally, they also detect pure rotational transitions from H_2 indicating presence of molecules along with the atomic jet. Line ratios from this source indicate that the atomic gas is characterized by an ionization fraction of 1%, which is considerably less as compared to ionization fraction of 10-20% measured in optical jets (Bacciotti et al. 1995). Initial jet composition is prescribed be 89% atomic, 10% molecular and 1% ionized, in qualitative agreement of above observational results.

The cooling in the reference jet is via molecular cooling prescription, whereby the initial hydrogen fractions are evolved using appropriate rate equations and with cooling contributions for abundant molecules like CO, OH etc. The final state (at time $\sim 1000 \text{ yr}$), i.e., density, temperature and velocity obtained from this run are given as inputs to the radiative transfer code to obtain the observational features corresponding to SiO molecule. For the radiative transfer calculation, the source in the reference run is stationary and the jet is in the plane of the sky ($\phi = 90^\circ$). A gaussian profile without any upper cutoff is used for the fractional abundance of SiO. Further, the shock velocity which determines the fractional abundance, v_s , is less than the jet velocity in the flow, such that their ratio δ is given by equation 8, where η is the density contrast as a function of height from the base of the jet.

6 RESULTS

6.1 Comparison of cooling prescription

We have done a comparison study of jet dynamics with various cooling prescriptions, which are described in Sect. 3. Figure 4 shows the density of the MHD jet at time ~ 1000 years for these different cooling prescriptions. For this study, we have chosen a density contrast at the base of $\eta = 10$ between the jet and ambient medium. It is clear from the figure 4, that the cooling plays a significant role in determining the structure of the jet. The jets with no or very little cooling are much wider compared to jets having dominant cooling.

For example, the adiabatic jet has the widest bow shock at its apex and has the most prominent shell of processed material, also known as the cocoon, around it. While the jet with atomic cooling has a rather conical jet head with significantly less cocoon surrounding it. The cocoon is almost absent from the narrow jet with tabulated cooling. Instead, the jet seems to form a very high density shell due to cooling of the processed ambient gas. Further, the jet with tabulated cooling is narrower than the jet with molecular cooling. This clearly shows the feedback of chemistry on the cooling function. The cooling terms for both these jets are the same to begin with, however, for the molecular jet the cooling terms evolve with jet dynamics as the fraction of various hydrogen species change over time. Whilst the terms remain fixed to initial values, shown in the fig 1, for the jet with tabulated cooling. Additionally, the material at the bow shock for the jet with tabulated and molecular cooling condenses forming dense knots. Such a condensation is caused due to thermal instability and is a typical feature of axi-symmetric radiative jets (see, for e.g, Blondin et al. 1990; Cerqueira & de Gouveia dal Pino 1999).

The dynamical states for each of this cooling prescriptions are then given as inputs to the radiative transfer code to obtain integrated $J = 2 \rightarrow 1$ SiO emission maps shown in figure 5. The differences in dynamical features are also reflected in the corresponding SiO emission maps. These maps are obtained assuming an angle of inclination of 90° using the top hat abundance profile with $\delta = 1$. They are then placed at a distance of 100 pc and convolved with a beam with FWHM of $2.0''$ in order to create the maps shown. The emission from the jet with atomic cooling is coming from the conical jet head and younger knots closer to base of the flow. Additionally, features in the shell at $Z \sim 60, 75$ also show evidence of faint emission. In case of the jet with power-law cooling the emission mostly arises from the internal knots. The emission coming from jets with tabulated and molecular cooling resembles that observed in young molecular outflows. Also in these outflows, strong emission arises from the condensation formed at the bow shock due to thermal instability.

In summary, different cooling prescriptions strongly influence the dynamics of MHD jet propagation in particular the thickness and structure of the bow shock. These dynamical differences are also reflected in SiO emission maps. The molecular cooling in our model consistently takes into account the feedback of temperature and density variation to evolve the chemical species unlike the tabulated cooling where the fraction of chemical species remains fixed. Thus, for our reference run we will adopt the molecular cooling prescription and compare results with observations. The properties of molecular cooling flows are described in details in the next section.

6.2 Molecular cooling and H_2 Chemistry

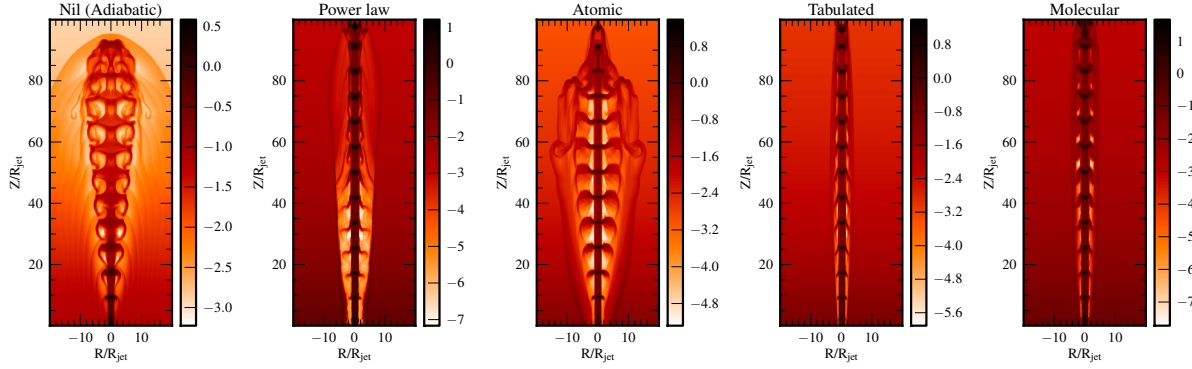
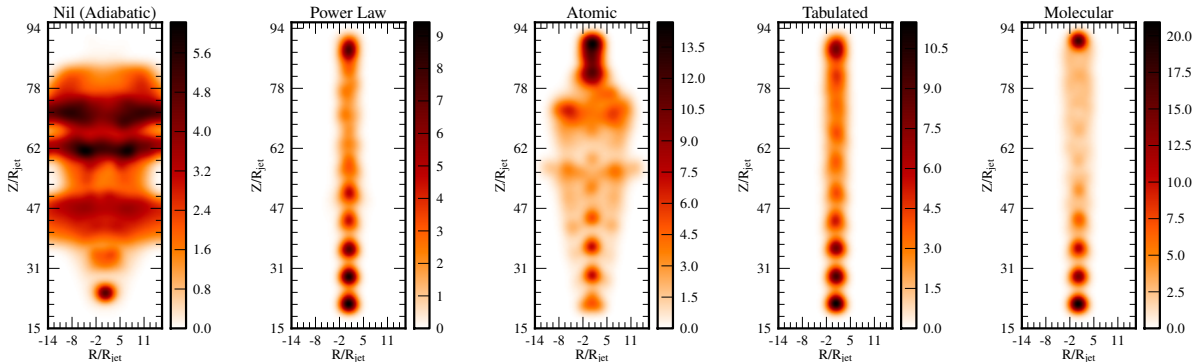
The molecular cooling in our model includes the evolution of H_2 chemistry along with contributions to cooling from fixed fractions of other molecules like CO, OH etc. Figure 6 shows the color composite image of various hydrogen fractions, (fHI (red), fH2 (green) and fHII (blue)), from the dynamical simulation with reference parameters. The jet beam is largely dominated by atomic hydrogen, while molecular hydrogen

Table 2. Summary from parameter runs. The parameter δ , is the ratio of shock to jet velocity and it depends on the density contrast η as shown in eq. 8

Run	Cooling Mode	η	Top Hat Profile $\delta = 1$		Gaussian Profile $\delta = 1$	
			$\int T_{\text{MB}} dV$ [K-km s $^{-1}$]	Δv [km s $^{-1}$]	$\int T_{\text{MB}} dV$ [K-km s $^{-1}$]	Δv [km s $^{-1}$]
adi10	Nil (Adiabatic)	10	2.91	>40	0.25	40.0
pow10	Power law	10	0.64	8.0	0.02	10.0
atm10	Atomic	10	2.04	36.0	0.58	38.0
atm2	Atomic	2	3.21	18.0	0.64	20.0
tab10	Tabulated	10	0.75	11.0	0.09	10.0
tab2	Tabulated	2	2.89	8.0	1.0	9.0
mol10	Molecular	10	1.10	10.0	0.1	11.0
mol3	Molecular	3	3.3	14.0	0.66	12.0

Table 3. Summary of radiative transfer runs with different SiO fractional abundance profiles for dynamical simulation with molecular cooling and $\eta = 3$. The integrated intensity assuming a single disk observation with a beam width of 15'' is listed along with the corresponding spectral width.

Profile	$\delta = v_s/v_{\text{jet}}$	$\int T_{\text{MB}} dV$ [K-km s $^{-1}$]	Δv [km s $^{-1}$]
Top Hat	1.0	3.3	14.0
Top Hat	$1/(1.0 + \eta(z)^{-0.5})$	4.9	14.0
Gaussian	1.0	0.66	12.0
Gaussian	$1/(1.0 + \eta(z)^{-0.5})$	1.1	12.0

**Figure 4.** Jet Volume Density for different cooling modes with $\eta = 10$.**Figure 5.** A plot of the integrated SiO J=2->1 emission from 5 models, each using a different method to calculate cooling and all with $\eta=10$.

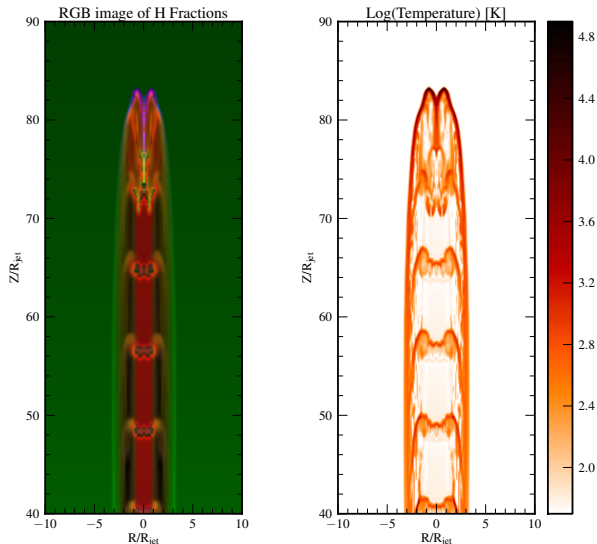


Figure 6. *Left* Color composite image of various hydrogen fractions, fHI (red), fH₂ (green) and fHII (blue), for the reference run. For better visualisation, the ionized hydrogen fraction is enhanced by a factor of 100. The temperature of the jet obtained from dynamical simulation is shown on the *right*.

is seen to be formed in internal knots and region that is thermally unstable. Ionized hydrogen is mainly formed at the tip of the bow. The highest temperature of ~ 50000 K is attained in our flow at the tip of the bow shock. While the temperature on the edges (i.e., interface between jet and the ambient medium) is lower than 5000 K. Also the relatively weaker shocks formed nearby knots do not heat up the material beyond 10^3 K.

The distribution of fractions of different hydrogen species along with temperature suggests that there are essentially three regions where chemistry is evolved due to shocks. They are : (1) The tip of the jet , (2) The edges of the jet and (3) intermediate knots. As the atomic jet propagates from the lower boundary into the cold molecular medium , it forms a strong shock resulting in forming a density and temperature discontinuity. Such a jump in dynamical quantities plays a crucial role in the evolution of chemistry. For example, temperatures beyond few 1000 K produced in the shocks could disassociate the molecules and can also lead to ionization if the temperature becomes larger than 10^4 K.

For the reference run, the effect of the shock in the dynamical evolution of the hydrogen fraction is presented in figure 7. The top panel of the figure shows the hydrogen number density in the jet. The fraction of all hydrogen forms are shown in bottom panels of figure 7 along two representative regions in the jet marked with the arrows. The left bottom panel shows the vertical distribution of temperature, molecular and atomic fraction at the interface of the knot and the ambient medium. The interaction of the knot with the medium raises that temperature to 1200 K and accumulates the matter so that the density increases up to 10^6 cm⁻³. Behind the shock as the material cools, atoms combine together to form molecules as seen in the increase of fH₂ from 0.44 to 0.52. Further away from the shock, atomic

and molecular hydrogen tend to reach a quasi equilibrium as their fractions reach a value of 0.5. The ionized fraction is extremely low in this region due to low temperatures. However at the bow-shock, temperatures rise up to 20000 K. Molecular hydrogen species are destroyed, while ionized hydrogen shows an increase in its fraction (figure 7). The peak in ionized fraction of 0.15 coincides with the peak in temperature profile as expected. The molecular fraction shows a considerable dip from 0.3 to 0.03 at this temperature before rising sharply in the ambient molecular medium.

6.3 Emission Maps, Spectra and PV diagrams

The output obtained from the radiative transfer calculation is a data cube with velocity being the third axis. This allows us to obtain spectra and position velocity diagrams from these data cubes. Figure 8 shows outputs from the data cube for SiO(2-1) in the reference run. The top left panel in the figure shows the emission map for the jet directed downwards. The notable features are the knots close to the base of the jet and the emission near the bow shock due to density enhancement by cooling instability. The PV diagram shown in the top right panel is obtained along the jet as indicated by the vertical magenta line in the left panel. The velocities are shown along the X-axis. High velocity features are clearly seen in regions corresponding to the knots in the emission maps. These features fade along the jet as the knots also disappear in the emission map. The region close to the bow shock also shows high velocity features.

The spectra at three different positions in the flow are shown in the bottom panel of figure 8 (they are marked with green crosses in top left panel). The knot closer to the base is the brightest showing a peak intensity of 25 K. The intensity decreases and reaches to about 10 K close to the bow shock. The line widths seen are typically around 5-10 km s⁻¹. These line widths increase substantially as the angle of inclination decreases. Figure 9 show the emission map, PV diagram and spectra for the same reference run but with angle of inclination of 45° respectively. The line widths now are typically of the order of 20 km s⁻¹. The PV diagrams in these runs are not longer symmetric. Instead, they show a distinct *zig-zag* pattern at each of the knots and region close to the bow shock.

6.4 SiO Abundance profile

The fractional abundance of SiO has been assumed to vary with shock velocity in a simplistic manner (see sec 4.3). In figure 10, we compare the maps for J = 2->1 emission at an inclination angle of 90° for three different abundance profiles and two different ratios of shock to jet velocities, δ . There is a striking difference with regards to emission from the internal knots in these images. Using the top hat profile and accounting for shock speeds (i.e. $\delta < 1$) results in emission from all the internal knots in the J=2->1 line. However, some of these knots are not observed when using the same top-hat profile but assuming the shock velocity to be same as the jet velocity (i.e., $\delta = 1$). Similar qualitative characteristics are seen in case of a gaussian abundance profile. In particular, the case with $\delta = 1$ only produces emission from the knot closest to the bow shock, while the internal knots

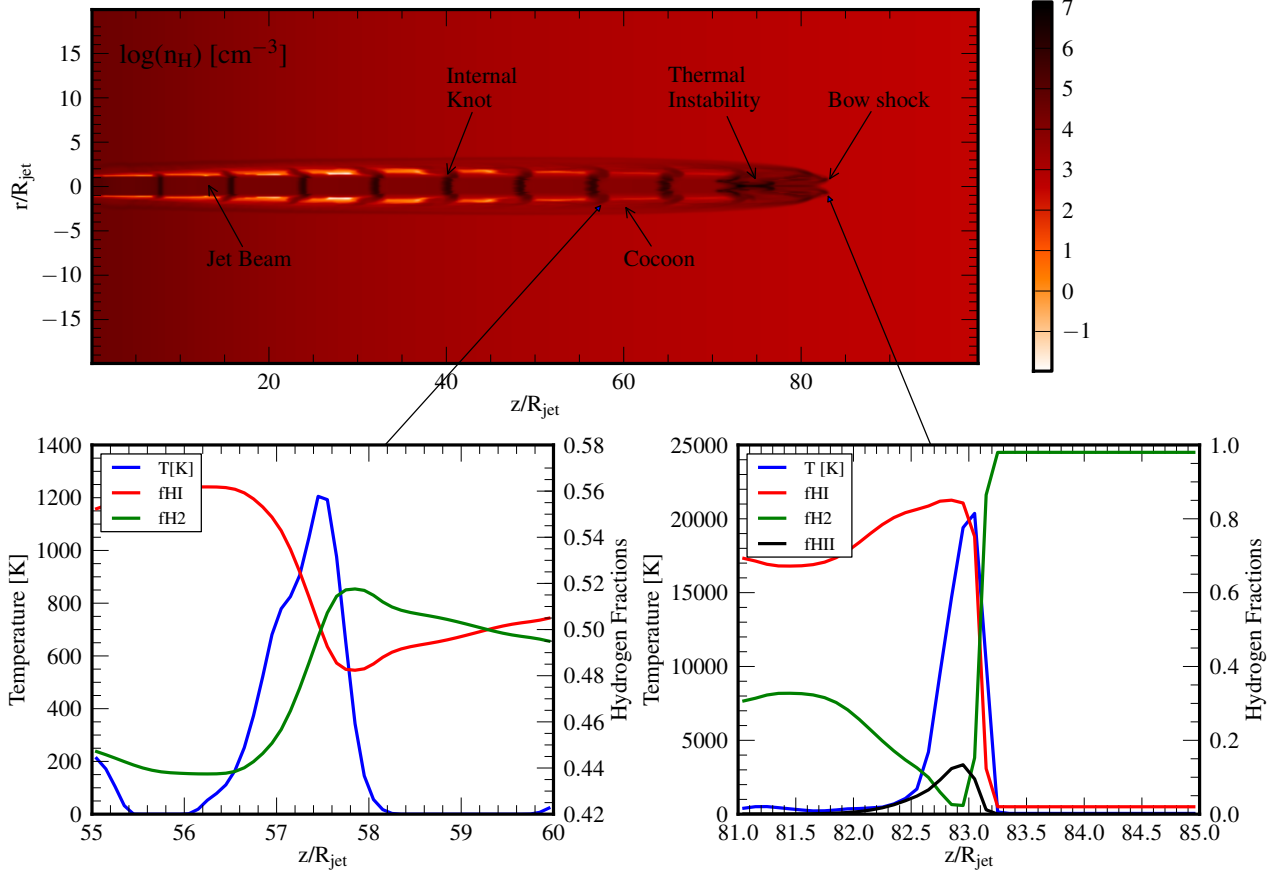


Figure 7. Dependence of hydrogen fractions on the temperature at two points in the flow, viz. the interface of the knot with molecular medium and at the bow shock.

do not show any appreciable emission. The step function and gaussian step (not shown) with $\delta = 1$ produces very similar features as that of the top hat profile with $\delta < 1$. Further, the emission from the knot closer to the bow shock varies considerably with different profiles and value of δ . It is the brightest for the case with a top-hat profile and $\delta < 1$. The peak emission and line widths at this knot are listed in table 3.

The dependence of emission on SiO abundance profile is expected due to the distribution of jet velocity obtained from dynamical simulations. We see that the velocity of internal knots lie around $70\text{--}90\text{ km s}^{-1}$, while the pulsed jet was injected with a mean of 100 km s^{-1} . The knots slow down during the evolutionary phase as they interact with the ambient medium. Interestingly, younger knots closer to the base of the jet are brighter compared to older ones further away from the jet (see panels 1 and 3 of fig 10). This is attributed to the fact that the ambient medium has a density gradient that goes as $\sim z^{-2}$. Thus, the younger knots suffer the most deceleration closer to the base of flow. This fact is taken into account when the shock velocity is consistently calculated using the density contrast and using a value of $\delta < 1$. This process is further validated by the lack of emission from internal knots in panel 3 of the fig 10.

Additionally, the internal knots show their distinct signatures in form of *Hubble wedges* as seen in the PV diagrams for these different profiles (see 6.3). Figure 11 shows

a zoomed in version of the bottom four internal knots in form of a PV diagram for these different abundance profiles. As expected, the signatures of knots is missing for the case with gaussian profile with $\delta = 1$. Further, the wedges formed in panels 1, 2 and 5 of the figure in general are slightly more extended as compared to those formed in panel 4. This is indeed because of the discontinuous nature of the top-hat abundance profile as the SiO is enhanced to a maximum abundance for all velocities between 20 and 100 km s^{-1} , which is not the case in a more continuous gaussian distribution.

7 ALMA VIEW

In order to see the interior structure of the molecular outflow and test the model predictions, high resolution interferometric observations are needed. We have performed synthetic Atacama Large Millimeter Array (ALMA) observations using the Common Astronomy Software Applications package (CASA). The output from the radiative transfer were scaled to a distance of 300pc and used as the sky models for observations of the J=2-1, J=5-4 and J=8-7 lines at frequencies of 86.85, 217.10 and 347.33 GHz, which fall in ALMA bands 3, 6 and 7, respectively. The observations were simulated using cycle 1 ALMA for 30 minutes total integration time, in the configurations c32-6, c32-4 and c32-3 for the three

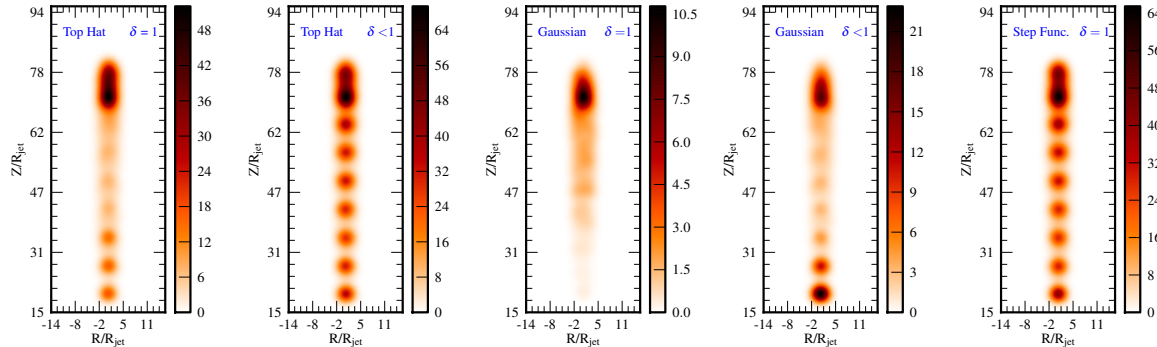


Figure 10. Variation of 2->1 SiO emission for runs with molecular cooling having different abundance profiles.

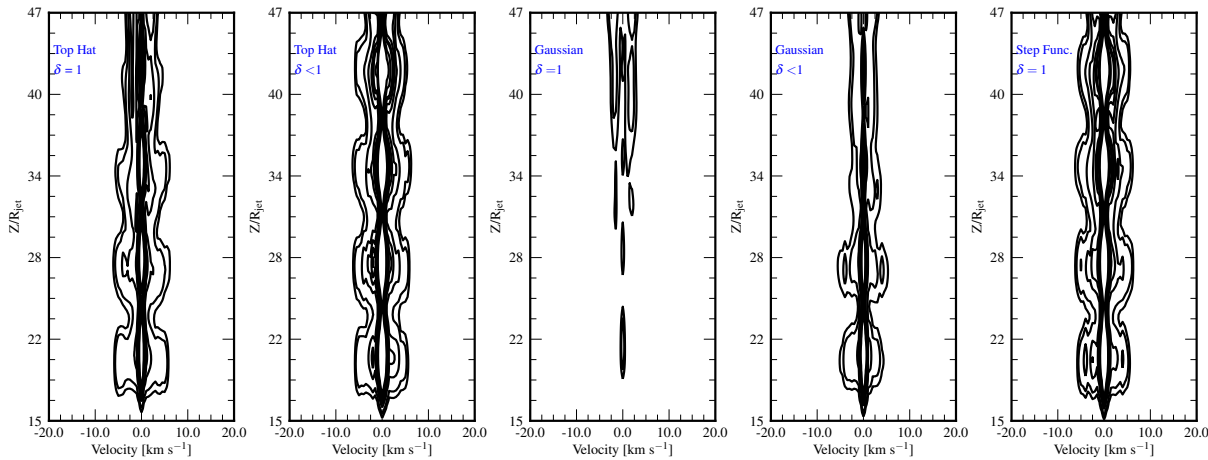


Figure 11. Position-velocity maps of SiO(2-1) for the internal knots produced in the model with reference parameters and different abundance profiles. The contours mark different levels of emission in Kelvins, viz., 0.2,0.6,1.0,1.4,1.8,2.0,3.0,4.0.

lines, giving beam sizes of $0.72''$, $0.47''$ and $0.58''$ and sensitivities of 0.05, 0.07 and 0.09 mJy/beam for the three lines (as calculated by the ALMA online sensitivity calculator) with velocity resolutions of ~ 1 km/s. Figure 12 presents the ALMA prediction obtained from our reference run. The left panel shows the integrated emission of SiO $J = 2-1$ line while the right shows the PV diagram for the same line and overlaid are the contours of SiO $J = 5-4$ and $J = 8-7$. The contour levels are marked on the color bar of each panel.

ALMA Cycle 0 observations have recently reported complex kinematic features of young bipolar molecular outflows. In particular, Arce et al. (2013) observed morphology, kinematics and entrainment of the HH 46/47 molecular outflow from a low mass nearby source ($d = 450$ pc) using CO(1-0). They find that the red lobe of the outflow exhibits a very complex structure with a collimated episodic wind, whereas the outflow in the blue lobe is consistent with a wide-angle wind model. Three major clumps in the red lobe along the outflow axis appear as *wedges* in the PV diagram (similar to that seen in the right panel of fig 12). A quantitative comparison is not possible due to the different molecule observed. Another source which is studied in details with ALMA band 7 is one of the most energetic, luminous molecular outflows

G331.512-0.103 (Merello et al. 2013). Observations of this outflow associated with a high mass star reveal a compact, extremely young bipolar outflow and a symmetric outflowing shell. Further, their PV diagrams with SiO and $H^{13}CO^+$ show a characteristic peak at -45 km s $^{-1}$ along the primary axis that could associated with a molecular *bullet* of high-velocity dense material as also found in our synthetic maps at inclination angles of 60° and 45° .

8 DISCUSSION

Here we compare our results with SiO observations of young low mass and high mass outflows.

8.1 EHV component and Molecular bullets

Multiline mm-wavelength surveys of SiO emission towards a sample of molecular outflows have shown that these outflows exhibit both low and high velocity SiO emission possibly arising from two distinct regimes. The slow component in the case of a typical outflow, L1448, is believed to arise from the shell of accelerated ambient gas with SiO abundance lower by two orders of magnitude than regions emitting the

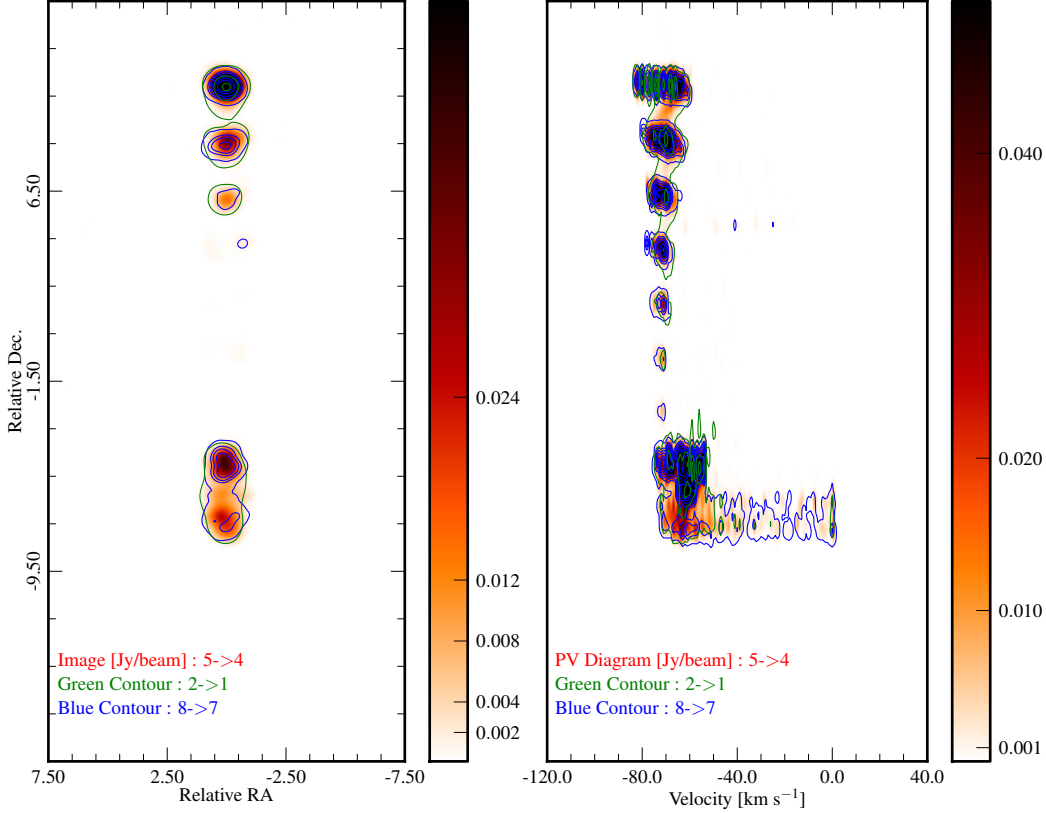


Figure 12. **Left:** The integrated intensity map of SiO(2-1), (5-4) and (8-7). The emission map shows the 5-4 line intensity (in units of $\text{Jy km s}^{-1}/\text{beam}$), the blue contours show the J=8-7 line intensity and the green contours show the J=2-1 line intensity. The jet is inclined at an angle of 60° . **Right:** The PV diagram taken along the axis of the jet for the 5-4 line (in units of Jy/beam), showing the higher J transitions highlighting the knots of the jet and broad emission at the bow shock. In both panels the ticks on the color bar represent the different contour levels.

high velocity component [Codella et al. \(1999\)](#). In addition, an interesting feature of EHV gas is seen in many young molecular outflows. The origin of the EHV component is still a mystery, however, recent high resolution observations show that EHV gas is seen in high density gas tracers (like CO and SiO) and the line have intensities ~ 0.1 K ([Tafalla et al. 2010](#)).

In IRAS 04166+2706, [Santiago-García et al. \(2009\)](#) have shown that the EHV CO(2-1) emission is mapping a jet-like feature that consists of a collection of discrete peaks symmetrically placed on both outflow lobes. This symmetry indicate that such EHV peaks might arise from events that took place near the central source and have since propagated in the flow ([Bachiller et al. 1990](#); [Tafalla & Bachiller 2011](#)). The dynamical model in conjunction with proper radiative transfer calculations presented here agrees very well with the above scenario. The *bullets* in our work are injected into the flow in a sinusoidal manner along with a collimated atomic jet. These pulsating ejections do interact with the medium via shocks and exciting high velocity gas. Including the cooling associated with molecules and the H_2 chemistry allows us to consistently identify the regions where molecular hydro-

gen is formed and disassociated (see fig. 7). The SiO emission that we obtain from our radiative transfer calculations is associated with regions slightly behind where the shocked H_2 gas is present as observed in case of L1157 molecular outflow [Gueth et al. \(1998\)](#). A contour map of SiO emission obtained from the reference run is shown in figure 13. Further, we find SiO emission coming from velocities of the order of $40\text{--}60 \text{ km s}^{-1}$ (see fig 9). Additionally, we see a distinct saw-tooth pattern in the PV diagrams from our models (see figs. 9 and 12). These predictions from our model very well resembles the characteristic features of EHV SiO emission seen in the majority of the outflows ([Santiago-García et al. 2009](#); [Tafalla & Bachiller 2011](#); [Arce et al. 2013](#)).

All of the above striking similarities from observations of EHV gas and synthetic spectra and PV diagrams gives a very formidable backing to the idea that such an emission could arise due to shock interactions of internal knots in the flow.

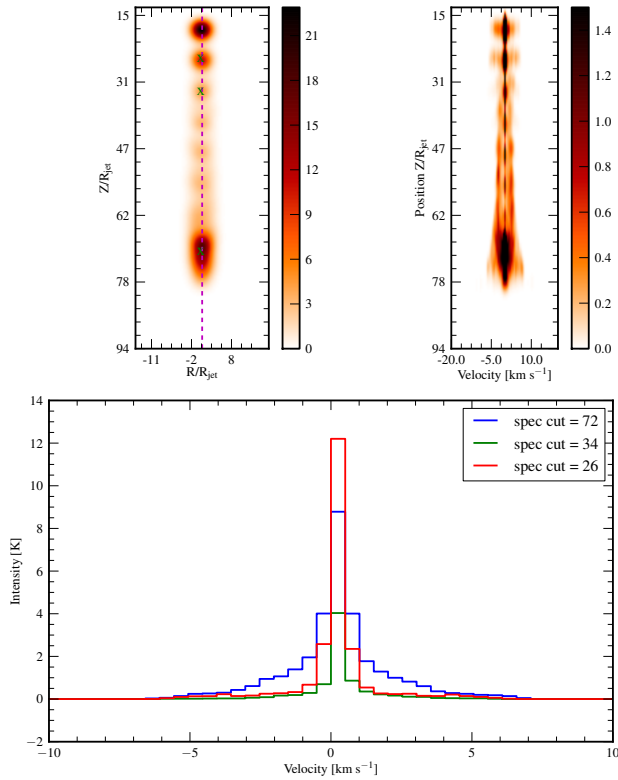


Figure 8. Integrated emission map (*top left*), PV diagram (*top right*) and spectra (*bottom*) for the 2->1 SiO transition for the reference run. The jet is assumed to be in the plane of sky implying an angle of inclination of 90° . The vertical *magenta dashed* line represents the cut for the PV diagram and green crosses marks the positions from which the spectra are taken.

8.2 Line transitions and ratio

Numerous molecular outflows with jet-like bullets have been observationally studied till date. In particular, H7-11 (Bachiller et al. 1998), IRAS 04166+2706 (Santiago-García et al. 2009; Tafalla et al. 2010), HH211 (Nisini et al. 2002) L1448 (Bachiller et al. 1991; Nisini et al. 2007; Tafalla et al. 2010) and L1157 (Nisini et al. 2007) have shown clear signatures of the EHV component. Among them, L1448, HH211 and L1157 have been studied in detail using an extensive multi-line survey of SiO. Such a multi-frequency analysis helps to understand the dependence of excitation conditions for these lines on velocity, based on existing shock models.

The most striking feature seen in the figure 13 is the progressive shift of emitting region from the interface to internal knots with increase in excitation energies of different lines. In particular, the lowest transition $J=1-0$ shows most of the emission coming from the interface between the jet and ambient medium, along with emission from the dense knots formed at the base of the flow. On the other hand, SiO (5-4) and (8-7) emission, is more concentrated in the inner jet regions and arise mainly from the shocks due to internal knots. Such a trend in emission with excitation energies coming from different SiO line transitions have been observed in young outflows (for e.g., L1448 bullets (Nisini et al. 2007), HH211 (Chandler & Richer 2001; Nisini et al. 2002; Hirano et al. 2006)). Further, the evolved post-shock

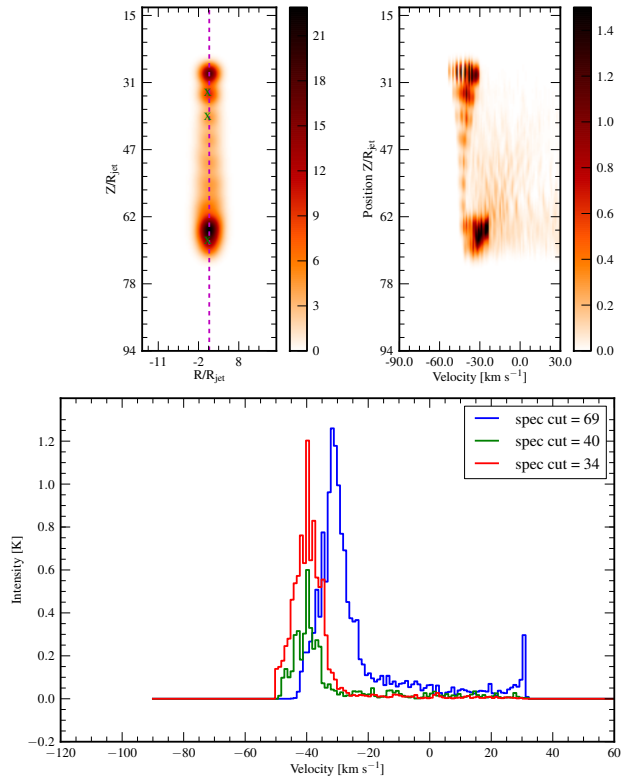


Figure 9. Same as figure 8 but with angle of inclination of 45° .

gas near the bow shock also show bright emission for these high J transitions. This gas is linked to the thermal instability associated with radiative jets (see section 6.1). The sub-structure seen close to the bow shock with high resolution does give a sense of clumpiness in the flow backing the suggestions to explain clumpy SiO emission has also been observed by Chandler & Richer (2001).

Nisini et al. (2007) have shown that the current plane-parallel shock models fit reasonably well the physical conditions traced by the SiO emission i.e., temperature $\lesssim 1000$ K and H_2 number density $\sim 10^5$ - 10^6 cm^{-3} , assuming optically thin emission. They can also fit the observed fractional SiO abundance of $\sim 10^{-7}$ in these outflows. However, they fail to predict all the line profiles and in particular their similarities for low and high excitation lines. Line emission for SiO from our model also traces similar physical environment. Fig. 7 shows that regions close to the internal knot have temperatures up to 1000 K and molecular hydrogen density of the order of 10^6 cm^{-3} (also see fig. 2). These are the regions where the bulk of the SiO emission is present, with fractional abundances between 10^{-6} to 10^{-8} . The line profiles shapes obtained from our study fit reasonable well with that observed by Nisini et al. (2007), especially for the bullets seen in L1448. Interestingly, in our models, the line profiles are equally broadened for low as well as high excitation lines. The top panel of fig. 14 shows spectra for three line transitions for the reference run but with an angle of inclination $\phi = 60^\circ$ and convolved with a single dish beam of $15''$ to simulate observed integrated intensities of L1448 bullets observed with large beams from JCMT and IRAM. Intensities predicted from our model (see table 3) lie within

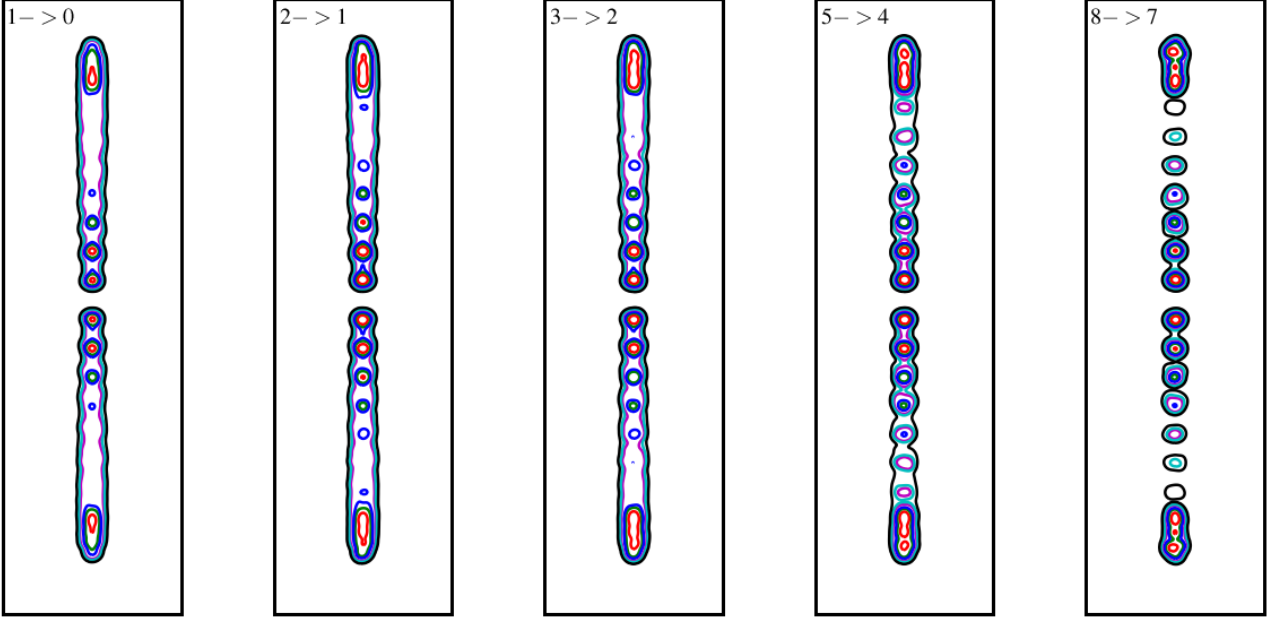


Figure 13. Symmetrical contour maps of multi-line integrated SiO emission convolved with a $2''$ beam obtained using parameters of the reference run. The contour colors represent different intensities in Kelvins, i.e., 20.0 (red), 10.0 (green), 5.0 (blue), 1.0 (magenta), 0.5 (cyan), 0.1 (black).

a factor of two from the observed values (Table 2 of [Nisini et al. 2007](#)).

The variation of integrated single dish emission with upper transition levels J_{up} for different abundance profiles is shown in the right panel of fig. 14. It is clear that the emission obtained using a top hat profile is brighter than the one obtained with a Gaussian SiO profile. However, curves obtained from both these profiles show a very similar shape of a distinct rise followed by a fall in integrated emission for higher transitions with a peak in emission for $J_{\text{up}} = 3$. These curves help to predict the hydrogen number density and temperature in outflows. Physical conditions in outflows can also be studied by estimation of line ratios. Values ≈ 1 for line ratios $\text{SiO}(8-7)/(5-4)$ and $\text{SiO}(5-4)/(2-1)$ have been found in HH212 ([Cabrit et al. 2007](#); [Lee et al. 2008](#)) and also for molecular outflows from massive young stellar object IRAS 17233-3606 ([Leurini et al. 2013](#)). The local velocity gradient (LVG) slab modeling with optically thin approximation were unable to produce these line ratios. In the present non-LTE radiative transfer modeling, no assumption of optical depths or photon escape probability are prescribed and line ratios are self consistently calculated and are shown in the bottom left panel of fig. 14. Their values lie very close to unity as indicated from observations. In summary, the shape, ratio and peak intensity of the spectra obtained from our model fit very well to observed values implying that SiO emission from our model is tracing the regions with right physical conditions that are required to emit SiO in the gas phase via shocks.

8.3 Slow Component and Grain Chemistry

We have presented a model that is able to explain the spectral characteristics of the SiO EHV component seen in several young outflows. The reference model consistently solves

for the H_2 chemistry in presence of appropriate cooling. The steady state temperature, density and velocities obtained from dynamical simulation is used as input in the non-LTE radiative transfer code to obtain SiO maps, spectra and PV diagrams. One essential ingredient required for the radiative transfer modeling is the SiO fractional abundance and its dependence on shock velocity. Though 1D models that study the formation of SiO in gas phase from grain-grain and grain-mantle collisions exists, their focus is mainly on weaker shocks ([Schilke et al. 1997](#); [Caselli et al. 1997](#); [Gusdorf et al. 2008](#)). The pulsating jet propagation model presented here have shock speeds reaching up to 100 km s^{-1} . We have used few simplified SiO abundance profiles as a function of shock velocity. Though the shape of the profile is uncertain, the upper and lower limits used are backed by observational evidences. Ideally, for a consistent dependence of SiO abundance on shock velocity, one would have to also solve for silicon and SiO chemistry in a manner similar to that of H_2 . However, such a numerically expensive model with complex chemistry is beyond the scope of this paper as this could imply to include dust grains and sputtering as well as grain-grain collisions (i.e. an MHD multi-fluid approach).

The model presented in this paper targets the very early phases of molecular outflows i.e., dynamical time scales of 1000 years. As discussed in sections above, the unique combination of pulsating jet with chemistry and cooling followed by non-LTE radiative transfer calculations has shown success in fitting the line shapes, integrated intensity and line ratios of SiO transitions arising from EHV gas. However, the synthetic spectra show no signatures of slow SiO component that accompanies EHV emission seen in many outflows (e.g., [Lefloch et al. 1998](#); [Codella et al. 1999](#)). The physical mechanism for the origin of the slow SiO component is still a matter of debate. [Codella et al. \(1999\)](#) suggest that it arises due to the slowing down of shocked gas as they age. The

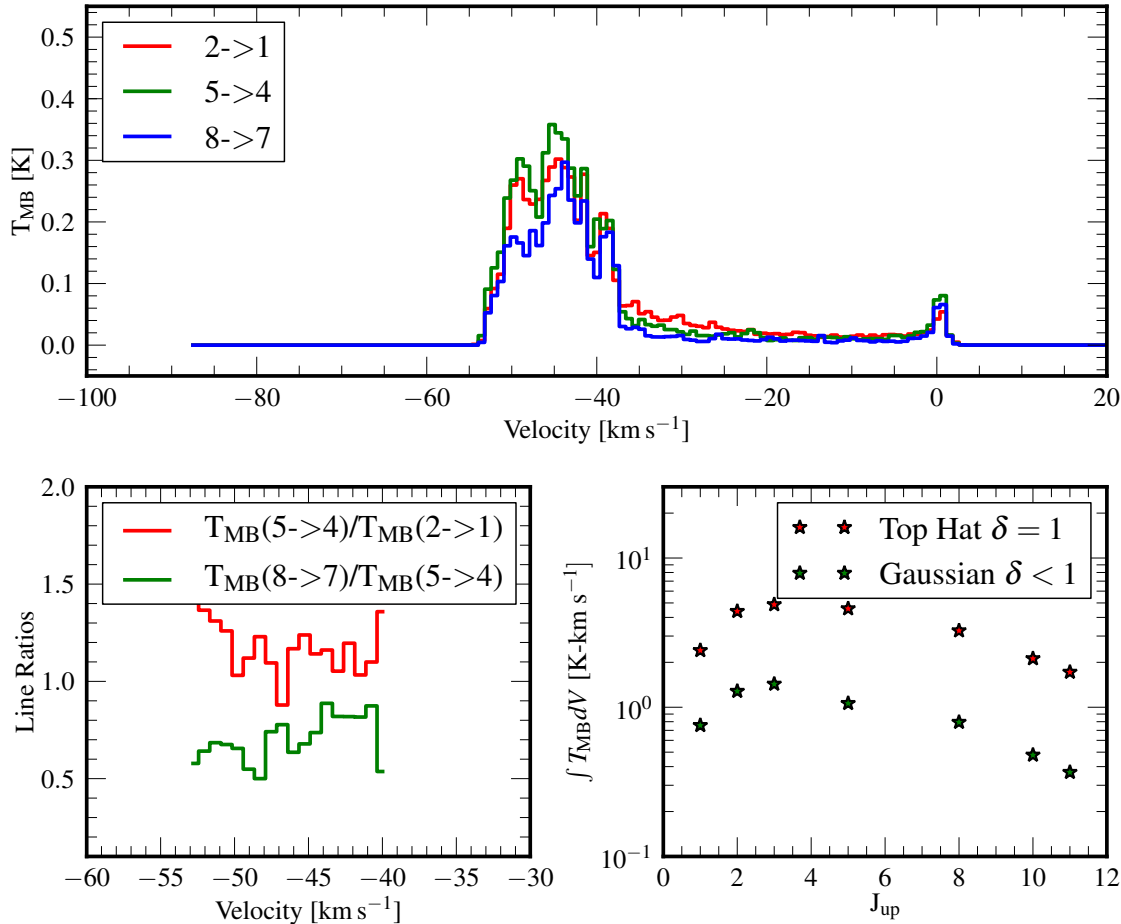


Figure 14. *Top* Line profiles in SiO (2-1), (5-4) and (8-7) at one the inner knots for the reference molecular cooling run with a top hat abundance profile and $\delta = 1$. The profiles are obtained when the angle of inclination is 60° with respect to line of sight. *Bottom left* Line intensity ratios SiO(8-7)/(5-4) and SiO(5-4)/(2-1), as a function of velocity. *Bottom right* Variation of integrated intensity with upper line transition J_{up} for two abundance profiles.

time scale estimated for the shocked gas to slow down is of the same order of magnitude as the SiO destruction time scale i.e., 10^4 years (Codella et al. 1999). In this case, we do not expect to see the slow velocity SiO component, as our models stop at ~ 1000 yr. However, we do see initial hints of slowing down of more evolved gas in terms of the velocity shift of about 7-10 km s⁻¹ in peak emission between that coming from the freshly formed internal knots close to the base of the flow and that from the more evolved gas near the bow shock. To ascertain this fact in more details, one would need to track the bow shock for 10^4 years using a larger simulation box and possibly with adaptive gridding which will be considered for future simulations. Such a long term evolution will also help to provide a numerical model for the formation of HH objects which are believed to be slowed down and more evolved forms of our young molecular bullets, as suggested by Norman & Silk (1979) and Hartigan et al. (1987).

An alternative hypothesis for the origin of the low veloc-

ity SiO component is that it could be formed by interaction of wider slow shocks with the ambient medium. Generally it is assumed that the silicon material comes from dust grain cores and that it is necessary to sputter or vaporise such cores to obtain some SiO in gas phase. However, some silicon material may be mixed with the ices on the dust grain surfaces (see discussion in Schilke et al. 1997). In such a scenario, shocks with speeds below 20 km s⁻¹ might inject a significant amount of silicon into the gas phase from the mantles, without completely destroying the grains. Jiménez-Serra et al. (2010) also found parsec-scale emission of SiO toward an infrared dark cloud suggesting that large scale shocks (may be triggered by cloud-cloud collisions Henshaw et al. 2013) may be responsible. Testing such scenarios is beyond the scope of the present model. One would not only need proper treatment of dust physics but also a two fluid model to study the impact of slow shocks in two dimensions. These models are indeed very important to study wide and slow emission from molecules like CO as seen in some

young outflows like L1157 (Gómez-Ruiz et al. 2013) and H₂O as seen from recent results of the Herschel-WISH survey (Tafalla et al. 2013).

9 CONCLUSION

We have performed MHD simulations of episodic radiative jet propagating with a typical speed of 100 km s⁻¹ into a cold, non-magnetized ambient molecular medium with a density gradient. The jet dynamical quantities are evolved in conjunction with different optically thin, non-equilibrium cooling prescriptions of varying complexities. The most complex is that of molecular cooling along with H₂ chemistry. This prescription allows us to track the formation and destruction of HI, HII and H₂ along with the flow dynamics. The final state of the jet obtained for each cooling model is then used as input into a non-LTE radiative transfer code to obtain SiO emission maps, spectra and PV diagrams. The main results obtained from our study are as follows :

- Different cooling prescriptions used for our model significantly influence thickness of the jet. An efficient mode of cooling does reduce the size of the cocoon and results in a more narrow jet. In addition, the bow shock structure differs with various cooling modes. Also, with realistic cooling functions one sees development of thermal instability at the jet head which also shows a significant emission in SiO along with young internal knots that are formed close to the base of the jet.

- Emission maps obtained from our reference run with molecular cooling show a distinctive collimated outflow structure. The physical regions responsible of SiO emission in such early outflows typically have molecular hydrogen densities $n \sim 10^6$ cm⁻³ and temperatures > 500 K which is consistent with properties deduced from LVG modeling of observational data of young outflows like L1448-mm.

- Our multi-line study of SiO clearly shows how different line transitions are sensitive to different regions in the jets. For example, the SiO J = 1- \rightarrow 0 transition is mostly excited due to the interaction of the jet with the ambient medium, while SiO J = 8- \rightarrow 7 trace the inner most jet regions as they are excited only in the internal knots. This finding very well supports the multi-line observational surveys done for young molecular outflows, particularly, HH 211.

- Single-dish synthetic spectra obtained from our model typically have intensity of 0.3 K and peak around 50 km s⁻¹ and have a typical line width of 20 km s⁻¹. Such modeled spectra are in excellent agreement with characteristic features of EHV emission of SiO seen in young molecular outflows. In addition, the line ratios T(8-7)/T(5-4) and T(5-4)/T(2-1), predicted from our models have values close to unity consistent with observations. Further, indications of the formation of the slow component due to the slowing down of the older knots is clearly seen as a shift of centroid velocities by 7-10 km s⁻¹ in the first 10³ years of evolution.

- The predicted PV diagrams from our models show a distinctive knot like features that are generally observed in outflows like IRAS 04166+2706.

- Emission from internal knots do depend on the chosen profile of the abundance. On one extreme where all the internal knots emit SiO with a step profile with $\delta = 1$ and a top-hat profile with $\delta < 1$, whereas, no emission is seen in

knots when a gaussian profile with $\delta = 1$ is used. For the remaining cases, we observe that emission mainly comes from knots close to the base of the flow and the condensation formed at the bow shock due to thermal instability.

- Predicted ALMA maps also show characteristic features that are consistent with young molecular outflows with EHV emission.

In summary, this work for the first time provides a model that explains the origin of EHV emission seen in SiO from the inner regions of young molecular outflows. The unique combination of axisymmetric jet propagation model with molecular cooling and non-LTE radiative transfer calculations can successfully reproduce most of the observed properties of SiO emission from young molecular outflows. This model provides an excellent template to compare current ALMA observations and can also predict signatures of thermal instabilities which can be tested with upcoming ALMA observations. In future, we would like to extend our model to full three dimensions with adaptive mesh refinement and evolve the jet for longer time scales to explore slow velocity component, precession and slew of other instabilities. Additionally, we would also like to have a better handle on SiO abundance not only from observations but also by including dust micro-physics in our model.

REFERENCES

- Abel T., Anninos P., Zhang Y., Norman M. L., 1997, *New A*, 2, 181
- Arce H. G., Goodman A. A., 2001a, *ApJ*, 554, 132
- Arce H. G., Goodman A. A., 2001b, *ApJ*, 551, L171
- Arce H. G., Mardones D., Corder S. A., Garay G., Noriega-Crespo A., Raga A. C., 2013, *ApJ*, 774, 39
- Arce H. G., Shepherd D., Gueth F., Lee C.-F., Bachiller R., Rosen A., Beuther H., 2007, *Protostars and Planets V*, pp 245–260
- Bacciotti F., Chiuderi C., Oliva E., 1995, *A&A*, 296, 185
- Bacciotti F., Ray T. P., Mundt R., Eisloffel J., Solf J., 2002, *ApJ*, 576, 222
- Bachiller R., 1996, *ARA&A*, 34, 111
- Bachiller R., Guilloteau S., Gueth F., Tafalla M., Dutrey A., Codella C., Castets A., 1998, *A&A*, 339, L49
- Bachiller R., Martin-Pintado J., Fuente A., 1991, *A&A*, 243, L21
- Bachiller R., Martin-Pintado J., Tafalla M., Cernicharo J., Lazareff B., 1990, *A&A*, 231, 174
- Bally J., 2007, *Ap&SS*, 311, 15
- Beuther H., Schilke P., Sridharan T. K., Menten K. M., Walmsley C. M., Wyrowski F., 2002, *A&A*, 383, 892
- Blandford R. D., Payne D. G., 1982, *MNRAS*, 199, 883
- Blondin J. M., Fryxell B. A., Konigl A., 1990, *ApJ*, 360, 370
- Brinch C., Hogerheijde M. R., 2010, *A&A*, 523, A25
- Cabrit S., Bertout C., 1992, *A&A*, 261, 274
- Cabrit S., Codella C., Gueth F., Nisini B., Gusdorf A., Dougados C., Bacciotti F., 2007, *A&A*, 468, L29
- Canto J., Raga A. C., 1991, *ApJ*, 372, 646
- Caselli P., 2011, in Cernicharo J., Bachiller R., eds, *IAU Symposium Vol. 280 of IAU Symposium, Observational Studies of Pre-Stellar Cores and Infrared Dark Clouds*. pp 19–32

- Caselli P., Hartquist T. W., Havnes O., 1997, *A&A*, 322, 296
- Cen R., 1992, *ApJS*, 78, 341
- Cerqueira A. H., de Gouveia dal Pino E. M., 1999, *ApJ*, 510, 828
- Chandler C. J., Richer J. S., 2001, *ApJ*, 555, 139
- Codella C., Bachiller R., Reipurth B., 1999, *A&A*, 343, 585
- Dionatos O., Nisini B., Cabrit S., Kristensen L., Pineau Des Forêts G., 2010, *A&A*, 521, A7
- Dionatos O., Nisini B., Garcia Lopez R., Giannini T., Davis C. J., Smith M. D., Ray T. P., DeLuca M., 2009, *ApJ*, 692, 1
- Dougados C., Bacciotti F., Cabrit S., Nisini B., 2010, in Garcia P. J. V., Ferreira J. M., eds, *Lecture Notes in Physics*, Berlin Springer Verlag Vol. 793 of *Lecture Notes in Physics*, Berlin Springer Verlag, *Deriving Physical Diagnostics from Observations*. p. 213
- Downes T. P., Cabrit S., 2003, *A&A*, 403, 135
- Downes T. P., Cabrit S., 2007, *A&A*, 471, 873
- Dutrey A., Guilloteau S., Bachiller R., 1997, *A&A*, 325, 758
- Flower D. R., Le Boulrot J., Pineau des Forêts G., Cabrit S., 2003, *MNRAS*, 341, 70
- Galli D., Palla F., 1998, *A&A*, 335, 403
- Glassgold A. E., Mamon G. A., Huggins P. J., 1991, *ApJ*, 373, 254
- Goddi C., Greenhill L. J., Chandler C. J., Humphreys E. M. L., Matthews L. D., Gray M. D., 2009, *ApJ*, 698, 1165
- Gómez-Ruiz A. I., Hirano N., Leurini S., Liu S.-Y., 2013, *ArXiv e-prints*
- Gueth F., Guilloteau S., 1999, *A&A*, 343, 571
- Gueth F., Guilloteau S., Bachiller R., 1998, *A&A*, 333, 287
- Guillet V., Jones A. P., Pineau Des Forêts G., 2009, *A&A*, 497, 145
- Gusdorf A., Cabrit S., Flower D. R., Pineau Des Forêts G., 2008, *A&A*, 482, 809
- Hartigan P., Frank A., Varnière P., Blackman E. G., 2007, *ApJ*, 661, 910
- Hartigan P., Raymond J., Hartmann L., 1987, *ApJ*, 316, 323
- Henshaw J. D., Caselli P., Fontani F., Jiménez-Serra I., Tan J. C., Hernandez A. K., 2013, *MNRAS*, 428, 3425
- Hirano N., Liu S.-Y., Shang H., Ho P. T. P., Huang H.-C., Kuan Y.-J., McCaughrean M. J., Zhang Q., 2006, *ApJ*, 636, L141
- Hollenbach D., McKee C. F., 1979, *ApJS*, 41, 555
- Jiménez-Serra I., Caselli P., Tan J. C., Hernandez A. K., Fontani F., Butler M. J., van Loo S., 2010, *MNRAS*, 406, 187
- Keto E., Caselli P., 2010, *MNRAS*, 402, 1625
- Konigl A., Pudritz R. E., 2000, *Protostars and Planets IV*, p. 759
- Lee C.-F., Ho P. T. P., Bourke T. L., Hirano N., Shang H., Zhang Q., 2008, *ApJ*, 685, 1026
- Lefloch B., Castets A., Cernicharo J., Loinard L., 1998, *ApJ*, 504, L109
- Leurini S., Codella C., Gusdorf A., Zapata L., Gómez-Ruiz A., Testi L., Pillai T., 2013, *A&A*, 554, A35
- Lloyd S., 1982, *Information Theory*, *IEEE Transactions on*, 28, 129
- Martin-Pintado J., Bachiller R., Fuente A., 1992, *A&A*, 254, 315
- Masson C. R., Chernin L. M., 1992, *ApJ*, 387, L47
- Masson C. R., Chernin L. M., 1993, *ApJ*, 414, 230
- Merello M., Bronfman L., Garay G., Lo N., Evans II N. J., Nyman L.-Å., Cortés J. R., Cunningham M. R., 2013, *ApJ*, 774, L7
- Mignone A., Bodo G., Massaglia S., Matsakos T., Tesileanu O., Zanni C., Ferrari A., 2007, *ApJS*, 170, 228
- Morse J. A., Heathcote S., Hartigan P., Cecil G., 1993, *AJ*, 106, 1139
- Mundt R., Brugel E. W., Buehrke T., 1987, *ApJ*, 319, 275
- Neufeld D. A., Dalgarno A., 1989a, *ApJ*, 340, 869
- Neufeld D. A., Dalgarno A., 1989b, *ApJ*, 344, 251
- Nisini B., Codella C., Giannini T., Richer J. S., 2002, *A&A*, 395, L25
- Nisini B., Codella C., Giannini T., Santiago Garcia J., Richer J. S., Bachiller R., Tafalla M., 2007, *A&A*, 462, 163
- Norman C., Silk J., 1979, *ApJ*, 228, 197
- Offner S. S. R., Lee E. J., Goodman A. A., Arce H., 2011, *ApJ*, 743, 91
- O'Sullivan J., Camenzind M., 2009, *Molecular Cooling in Large Scale Simulations of Protostellar Jets*. pp 453–458
- Panoglou D., Cabrit S., Pineau Des Forêts G., Garcia P. J. V., Ferreira J., Casse F., 2012, *A&A*, 538, A2
- Podio L., Bacciotti F., Nisini B., Eisloffel J., Massi F., Giannini T., Ray T. P., 2006, *A&A*, 456, 189
- Powell K. G., Roe P. L., Linde T. J., Gombosi T. I., de Zeeuw D. L., 1999, *Journal of Computational Physics*, 154, 284
- Raga A., Cabrit S., 1993, *A&A*, 278, 267
- Raga A. C., Taylor S. D., Cabrit S., Biro S., 1995, *A&A*, 296, 833
- Rathborne J. M., Simon R., Jackson J. M., 2007, *ApJ*, 662, 1082
- Rawlings J. M. C., Redman M. P., Carolan P. B., 2013, *MNRAS*, 435, 289
- Ray T., 2012, in *EAS Publications Series Vol. 58 of EAS Publications Series*, *Outflows from young stars : The Rosetta stone of astrophysical Jets?*. pp 105–112
- Santiago-García J., Tafalla M., Johnstone D., Bachiller R., 2009, *A&A*, 495, 169
- Schilke P., Walmsley C. M., Pineau des Forêts G., Flower D. R., 1997, *A&A*, 321, 293
- Shang H., Allen A., Li Z.-Y., Liu C.-F., Chou M.-Y., Anderson J., 2006, *ApJ*, 649, 845
- Shu F. H., Ruden S. P., Lada C. J., Lizano S., 1991, *ApJ*, 370, L31
- Smith M. D., Rosen A., 2003, *MNRAS*, 339, 133
- Stone J. M., Hardee P. E., 2000, *ApJ*, 540, 192
- Tafalla M., Bachiller R., 2011, in Cernicharo J., Bachiller R., eds, *IAU Symposium Vol. 280 of IAU Symposium*, *Molecules in Bipolar Outflows*. pp 88–102
- Tafalla M., Liseau R., Nisini B., Bachiller R., Santiago-García J., van Dishoeck E. F., Kristensen L. E., Herczeg G. J., Yıldız U. A., 2013, *A&A*, 551, A116
- Tafalla M., Santiago-García J., Hacar A., Bachiller R., 2010, *A&A*, 522, A91
- Vaidya B., Fendt C., Beuther H., Porth O., 2011, *ApJ*, 742, 56
- Vaidya B., Goddi C., 2013, *MNRAS*, 429, L50
- Woodall J., Agúndez M., Markwick-Kemper A. J., Millar

T. J., 2007, A&A, 466, 1197

Ziurys L. M., Friberg P., Irvine W. M., 1989, ApJ, 343, 201